Volume 9
Number 3
March 2024
Pages 237–325

MSDE

Molecular Systems Design & Engineering

rsc.li/molecular-engineering

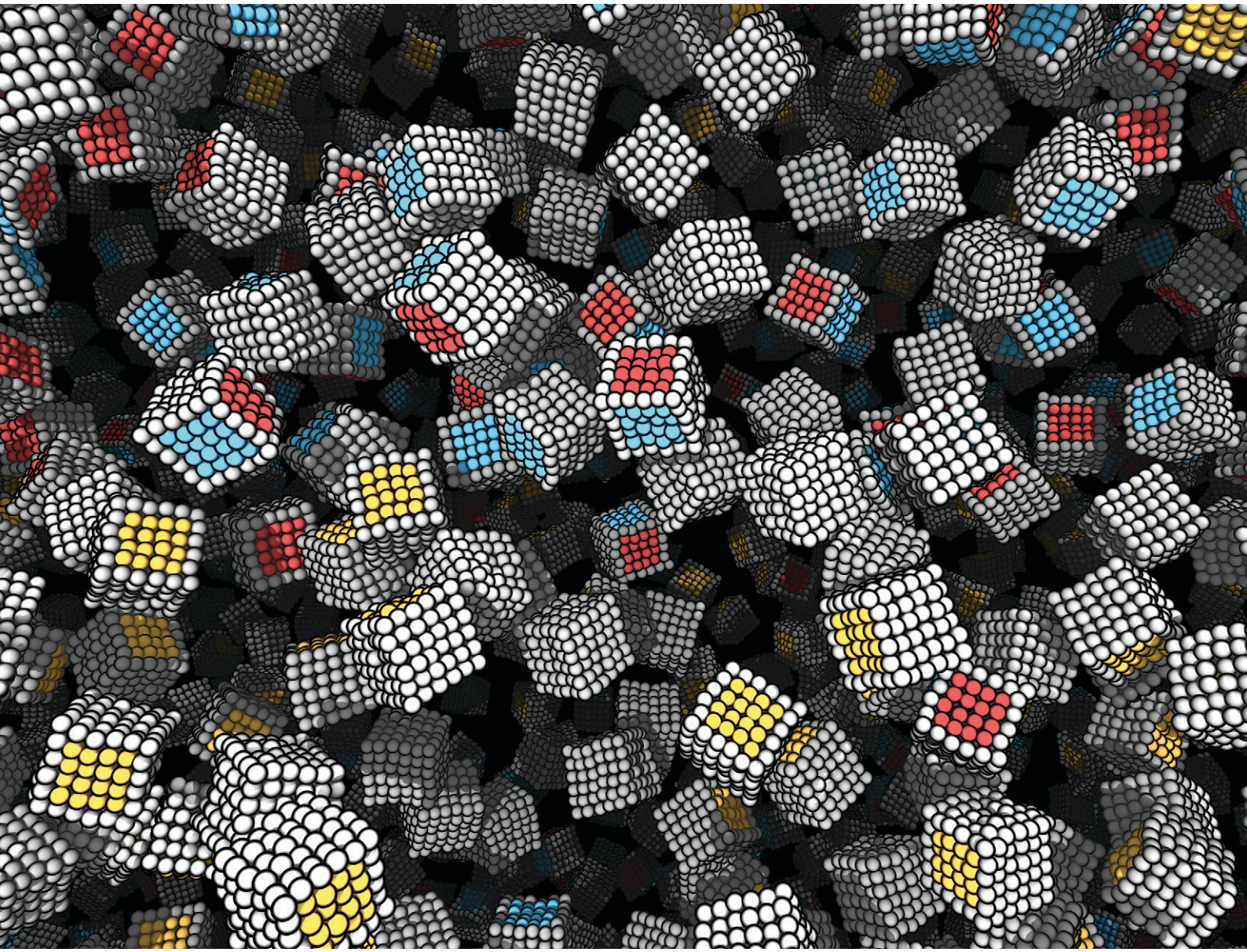

ISSN 2058-9689

ROYAL SOCIETY OF CHEMISTRY

PAPER

Yusei Kobayashi *et al.*

Shear-induced structural and viscosity changes of amphiphilic patchy nanocubes in suspension

IChemE ADVANCING CHEMICAL ENGINEERING WORLDWIDE

MSDE

PAPER

View Article Online
View Journal | View Issue

Cite this: *Mol. Syst. Des. Eng.*, 2024, **9**, 254

Shear-induced structural and viscosity changes of amphiphilic patchy nanocubes in suspension

Takahiro Ikeda, Yusei Kobayashi * and Masashi Yamakawa

Structure formation and rheological properties of amphiphilic patchy nanocubes in equilibrium and under shear were investigated using hybrid molecular dynamics simulations combined with multiparticle collision dynamics that consider hydrodynamic interactions. The relationship between complex self-assembled structures and the resulting macroscopic properties has not yet been examined because of the computational complexity these multiscale problems present. The number and location of solvophobic patches on the amphiphilic nanocubes were varied at several colloid volume fractions in the liquid regime. For a pure suspension of one-patch cubes, the nanocubes self-assemble into dimers in the equilibrium state because bonded one-patch cubes have no exposed solvophobic surfaces. At low shear rates, small dimers undergo shear-induced alignment along the flow direction. This results in shear-thinning accompanied by slightly higher shear viscosity (≈15%) than homoparticle dispersions of the same concentration. As the shear rate increases further, the suspensions exhibit Newtonian-like behavior until the cluster disintegrates, followed by shear thinning with breakdown into individual cubes. For binary mixtures of one- and two-patch nanocubes, the resulting cluster shapes, which include elongated rods and fractal objects, can be controlled by the patch arrangements on the two-patch cubes. Interestingly, despite the differences in the shape and resistance of the clusters, two different mixtures undergo a similar increase in the shear viscosity (≈35%) compared to the homoparticle dispersions, to essentially exhibit rheological behavior similar that of a pure suspension of one-patch cubes. Our findings provide new insights into the correlation between microscopic (design of patchy cubes), mesoscopic (self-assembled structures), and macroscopic (viscosity) properties, and are also valuable for identifying the synthesis conditions required to realize novel materials with the desired properties and functionalities.

Received 20th December 2023,
Accepted 17th January 2024

DOI: 10.1039/d3me00198a

rsc.li/molecular-engineering

Design, System, Application

Recent advances in the controlled synthesis of nanoparticles have resulted in a large variety of anisotropic nanoparticles with both highly tailored interactions (patches) and strict shape control. The combination of interaction and shape anisotropy is a powerful approach for achieving targeted self-assembled structures and accessing emerging materials. Our study demonstrates the correlation between the design of patchy nanocubes, their self-assembled structures including shear-induced structural changes, and the rheological properties of suspensions. For binary mixtures of one- and two-patch nanocubes, the resulting cluster shapes, which include elongated rods and fractal objects, can be controlled by the patch arrangements on the two-patch cubes. We found a significant correlation between the rheological properties of patchy nanocubes and both the cluster size and the orientational ordering of clusters. The unique aggregation morphologies and rheological behaviors of such patchy nanocubes cannot be achieved not only with purely repulsive or attractive nanocubes, but also with patchy spheres or nanorods. The identified relationship between self-assembly and rheological property contributes to the development of advanced functional materials such as viscosity modifiers and emulsion stabilizers at the molecular-level. Our findings are also valuable for identifying the synthesis conditions required to realize novel materials with the desired properties and functionalities.

1 Introduction

Colloidal self-assembly has attracted much attention in both science and industry owing to their potential applications, *e.g.*, oil recovery,[1–3] drug delivery,[4–6] catalysis,[7–9] and biosensing.[10–12] The collective and enhanced dynamics and properties of these materials arise not only from the chemical nature of the nanoparticles, but also from their complex self-assembled structures. Therefore, it is important to clarify the relationship between the self-assembled structures and the resulting macroscopic properties to produce materials with the desired properties and functionalities.

A promising method for controlling the self-assembled structure of colloidal particles is to introduce anisotropy into

Faculty of Mechanical Engineering, Kyoto Institute of Technology, Matsugasaki, Sakyo-ku, Kyoto 606-8585, Japan. E-mail: kobayashi@kit.ac.jp

the interaction forces. Recent advances in the controlled synthesis of nanoparticles have resulted in nanoparticles with highly localized and tailored interactions. A general approach toward this end involves the formation of nanoparticles with highly selective directional interactions by grafting complementary DNA chains onto a particle surface.[13–17] Alternatively, surface patterning *via* site-selective surface modification is a versatile strategy for inducing directional interparticle interactions.[18–21] These colloidal particles with site-specific directional interactions are referred to as "patchy particles" and their patches serve as a program for self-assembly defined by the pattern on the surface of the particle.[22,23] For example, metallic nanoparticles with regioselective DNA patches self-assemble into dimers, trimers, and pentamers, which is not observed for isotropic particles.[24] Binary mixtures of two different types of patchy tetrahedral particles can thermodynamically and kinetically enhance the formation of diamond lattices.[25]

Shape anisotropy is a key factor in colloidal self-assembly.[26–28] Nonspherical particles are ubiquitous in nature, such as discotic montmorillonite[29,30] and rod-shaped tobacco mosaic viruses,[31,32] and have been well studied as model shapes. Numerous efforts have been made to develop synthetic strategies for anisotropic colloids with nonspherical shapes, which allow the preparation of a large variety of anisotropic colloids with strict size and shape control.[26,33] Faceted nanoparticles are attractive candidates for the fabrication of unique and complex nanostructures.[34–37] Among these, a nanocube is one of the simplest shapes and a prime example of a space-filling polyhedron. The structural formation and physical properties of purely repulsive hard cubes have been studied extensively.[38–41] For instance, Cwalina *et al.* investigated the rheology of concentrated suspensions of cubic aluminosilicate zeolite particles, and related their measured properties to suspensions of spherical particles.[41]

The combination of interaction and shape anisotropy is a powerful approach for achieving targeted self-assembled structures and accessing emerging materials. Various approaches such as the DNA origami technique[42–44] and grafting DNA chains onto the surface of a nanocube[45,46] have been proposed experimentally for the realization of nanocubes with patterned surfaces. However, a large number of parameters influence the self-assembly of patchy nanocubes, *e.g.*, the interaction potential, interaction strength, number and location of patches, and concentration. Therefore, the systematic experimental exploration of an enormous parameter space would be highly challenging. In this regard, coarse-grained molecular simulations are powerful tools that can provide molecular-level interpretations of experimental results and allow efficient exploration of the parameter space. For example, Monte Carlo (MC) simulations of polymer-grafted nanocubes were performed to investigate the assembly mechanism in detail, and it was found that the free energy barriers between metastable states depend on the interaction strength and surface roughness of the nanocubes and steric repulsion from the grafts.[47,48] In addition, we recently investigated the equilibrium self-assembly of amphiphilic cubes and the assembly dynamics under shear using a combination of molecular dynamics (MD) and kinetic MC simulations.[49,50] Previous studies have focused on the self-assembly behavior induced by the design of nanocubes, but have not investigated the relationship between complex self-assembled structures and the resulting macroscopic properties owing to the computational complexity multiscale problems involve.

In this study, we performed hybrid MD simulations combined with multiparticle collision dynamics (MPCD) to investigate the structural formation and rheological properties of amphiphilic patchy nanocubes at equilibrium and under shear conditions. We systematically varied the number and location of solvophobic patches on amphiphilic nanocubes at different colloidal volume fractions in the liquid regime of the phase diagram and analyze the correlation between the microscopic (design of patchy cubes), mesoscopic (self-assembled structures), and macroscopic (viscosity) phenomena.

2 Methods and models

We use the MD simulations coupled to the MPCD.[51–53] Based on our previous works,[49,50] a discrete particle model was used for the nanocubes, which can be considered as coarse-grained models for DNA-functionalized nanoparticles, allowing only face-to-face interactions (Fig. 1(a)). Note that here, the possibility exists that the coarse-graining procedures such as our simulation models instead of precision macromolecules called "giant molecules",[54] may not be suitable for understanding protein self-assembly, because the behaviors of proteins, *e.g.*, protein–protein complex and their assembling

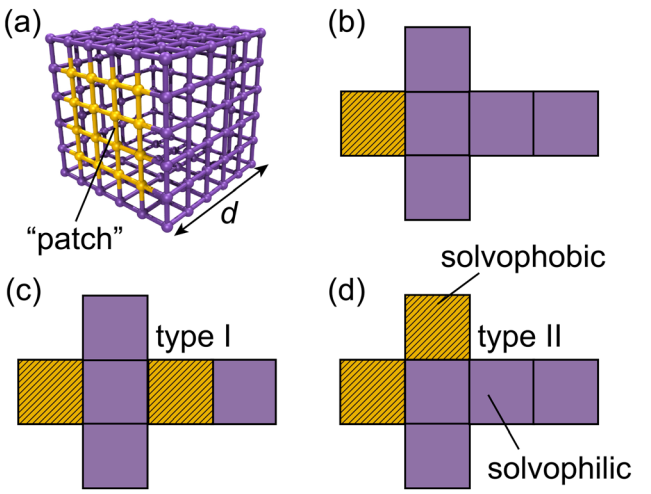

Fig. 1 (a) Discrete particle model of a (one-patch) cubic cube with diameter $d = 5a_v$. The N_v vertex particles and bonds between nearest neighbors are shown (diametric bonds have been omitted for clarity). (b–d) Unfolded representations of terminal one-patch cube and two-patch cubes. In all panels, solvophilic patches are colored in purple and solvophobic ones in yellow. Snapshot rendered using Visual Molecular Dynamics (version 1.9.4).[56]

process are more complex than that of DNA-functionalized nanoparticles. Each nanocube consists of N_v vertex particles of diameter a_v and mass m_v. The vertex particles are placed on the cube surface on a quadratic lattice and connected to their nearest neighbors and with the diametrically opposite particle through a harmonic potential U_b:

$$U_b(r_{ij}) = \frac{k}{2}(r_{ij} - r_0)^2, \quad (1)$$

where k is the spring constant, r_{ij} is the distance between two particles i and j, and r_0 is the equilibrium bond distance. The spring constant is set to $k = 5000k_BT/a_v$ to maintain a (nearly) rigid shape of the colloid[49,50,52,55] with Boltzmann's constant k_B and temperature T. The cube diameter was set to $d = 5a_v$ with a lattice spacing of $5/6a_v$, resulting in $N_v = 152$ vertex particles per nanocube. The mass of the nanocube is then $m = N_v m_v$.

As shown in Fig. 1(b and c), we consider suspensions of (nearly) hard colloidal cubes, with between one and two solvophobic faces (so-called "patches") while the remaining faces are solvophilic. Each solvophobic patch comprised 16 vertex particles (Fig. 1(a)). A total of six and 15 different possibilities exist for arranging the hydrophobic patches on one- and two-patch cubes, respectively; however, only a small subset of patch arrangements is geometrically distinct. In the following, we refer to the two different realizations as type I and II, as indicated in Fig. 1(c) and (d). We introduce the standard Lennard-Jones potential (U_{LJ}) between the vertex particles of solvophobic patches to mimic the (effective) solvent-mediated attraction, and U_{LJ} is given as

$$U_{LJ}(r_{ij}) = \begin{cases} 4\varepsilon_{ij}\left[\left(\frac{a_v}{r_{ij}}\right)^{12} - \left(\frac{a_v}{r_{ij}}\right)^{6}\right], & r_{ij} \le r_{cut} \\ 0, & r_{ij} > r_{cut} \end{cases} \quad (2)$$

where r_{ij} denotes the distance between vertex particles i and j, $\varepsilon_{ij} = 1.0k_BT$ is the interaction strength, and $r_{cut} = 3.0a_v$ is the cutoff radius. The excluded volume interactions between solvophilic vertex particles and between solvophilic and solvophobic vertex particles were modeled using the purely repulsive Weeks–Chandler–Andersen potential U_{WCA}:[57]

$$U_{WCA}(r_{ij}) = \begin{cases} U_{LJ}(r_{ij}) + \varepsilon, & r_{ij} \le 2^{1/6}a_v \\ 0, & r_{ij} > 2^{1/6}a_v. \end{cases} \quad (3)$$

To focus on the self-assembly of amphiphilic patchy nanocubes into finite-sized aggregates, we simulated binary mixtures of amphiphilic nanocubes, that is, systems consisting of a fraction f of two-patch cubes, with the remaining fraction $1 - f$ consisting of one-patch cubes. In this study, two different fractions, namely $f = 0.0$ and $f = 0.5$ are considered. The edge length of the cubic simulation box was set to $L = 80a_v = 16d$ and periodic boundary conditions were applied in all three Cartesian directions to mimic the bulk conditions. The initial configurations were prepared by placing the nanocubes at random positions and orientations in the simulation box, while avoiding any overlap between the constituent particles. Three different volume fractions, $\phi \equiv N_v d^3/L^3 = 0.028$ (115), 0.056 (230), and 0.112 (459), where the numbers in parentheses denote the total number of nanocubes in the simulation box.

In the MPCD technique, the solvent is modeled as point particles of unit mass m_s propagated by sequential streaming and stochastic collision steps. During the streaming step, the solvent particles move ballistically for a period Δt_{MPCD} according to the following equation of motion:

$$\mathbf{r}_i(t + \Delta t_{MPCD}) = \mathbf{r}_i(t) + \mathbf{v}_i(t)\Delta t_{MPCD}, \quad (4)$$

where Δt_{MPCD} denotes the time step of the MPCD algorithm. Following the streaming step, the simulation box was first divided into regular cubic cells with an edge length a_v, and the solvent particles in the same cell then underwent stochastic collision. In this study, we used the stochastic rotation dynamics (SRD) variant of the MPCD algorithm,[51] where the solvent particles in each cell are rotated relative to the center-of-mass velocity of the cell by a fixed angle α around a randomly oriented axis:

$$\mathbf{v}_i(t + \Delta t_{MPCD}) = \mathbf{u}(t) + \Omega(\mathbf{v}_i(t) - \mathbf{u}(t)). \quad (5)$$

where $\mathbf{u}(t)$ is the center-of-mass velocity of the cell to which particle i belongs and Ω is a norm-conserving rotation operator. This procedure conserves energy, mass, and linear momentum at the cell level; thus, the Navier–Stokes equation is fulfilled, and hydrodynamic interactions are reproduced down to the size of a collision cell.[58,59] The coupling of the solvent to the solute (vertex particles) was achieved through participation in the collision step. To avoid the lack of Galilean invariance, all collision cells were shifted along a randomly selected direction, with components drawn uniformly on $[-a_v/2, +a_v/2]$ before each collision step.[60]

The choice of MPCD parameters in this study was inspired by our previous work.[50,61,62] Thus, the (average) solvent number density, collision angle, and time step for the MPCD algorithm were set as $\rho = 10a_v^{-3}$, $\alpha = 130°$, and $\Delta t_{MPCD} = 0.1\tau$, respectively. The temperature was maintained at $k_BT = 1$ by using a cell-level Maxwellian thermostat.[58] For the conventional MD step, we used a Verlet integration scheme[63] with a time step $\Delta t_{MPCD} = 0.005\tau$ and a unit of time $\tau = \sqrt{m_s/(k_BT)}a_v$. The mass of the vertex particles was set to the (average) mass of a collision cell filled with solvent particles only; thus, $m = m_s\rho_s a_v^3 = 10m_s$. These MPCD parameters provided a solvent viscosity of $\eta_s = 8.72\varepsilon\tau/a_v^3$. Periodic boundary conditions were applied to all three dimensions. All simulations were performed using the HOOMD-blue software package (v. 2.9.6)[64–67] with the "azplugins" extension (v. 0.6.2)[68] for generating shear flow.

3 Results and discussion

3.1 Homoparticle dispersions

To validate our algorithms, we begin with homogeneous (without patchy faces) nanocubes and compare the zero-shear viscosity η_0 of homogeneous cubic dispersions with the

predicted data from the estimated regression equations. In principle, the Green–Kubo relations can be used to determine η_0 through equilibrium simulations. However, our previous simulations of spherical colloid dispersions[61] indicated that applying a weak shear resulted in a significantly improved signal-to-noise ratio. Thus, we employed the reverse perturbation method[69] to generate shear flow in the system. In this technique, the simulation box is first subdivided into equally sized slabs in the gradient (z) direction of the flow. Subsequently, the most negative momentum of the particles in the $z = +L_z/4$ slab and the most negative momentum of the particles in the $z = -L_z/4$ slab were swapped. The shear strength can be controlled by tuning the number of momentum swaps in a step or the momentum swap frequency Δt_{swap}. The resulting shear viscosity η is obtained by

$$\eta = \frac{\langle \sigma_{xz} \rangle}{\dot{\gamma}}, \tag{6}$$

where $\langle \ldots \rangle$ represents the time average, $\dot{\gamma}$ is the shear rate calculated from the slope of the linear velocity profile that develops in the steady state, and σ_{xz} is the shear stress given by

$$\sigma_{xz} = \frac{\Delta p_z}{2\Delta t_{\text{swap}} L^2}, \tag{7}$$

where Δp_z is the total exchange momentum in a single step. For a well-dispersed colloidal suspension, the zero-shear viscosity η_0 can be described by the following equation:[41,70]

$$\eta_0 = \eta_s(1 + k_E\phi + k_H\phi^2 + \text{higher order terms}), \tag{8}$$

where k_E is the Einstein coefficient, which is independent of the particle size and size distribution, and k_H, known as the Huggins coefficient, is related to the contribution of hydrodynamic interactions between pairs of particles to η_0.[70] For a dilute suspension of hard spheres, Einstein[71,72] determined the value of $k_E = 2.5$.

In addition, the flow behavior of suspensions of shape-anisotropic particles has recently been studied. For instance, Mallavajula *et al.*[73] studied through simulations and experiments the dilute dispersions of Fe_3O_4 nanocubes in the dilute limit and found a modified Einstein coefficient that is independent of the particle size and size distribution:

$$\eta_0 = \eta_s(1 + 3.1\phi). \tag{9}$$

A recent experimental study of semidilute suspensions of cubic aluminosilicate zeolite particles by Cwalina *et al.*[41] showed that the ϕ^2 term is necessary to account for the concentration dependence of viscosity. The values of k_E and k_H, obtained by regression from their experiments were 3.5 ± 0.3 and 23.7 ± 3.0, respectively, thus η_0 is given as:

$$\eta_0 = \eta_s(1 + (3.5 \pm 0.2)\phi + (23.7 \pm 3.0)\phi^2). \tag{10}$$

Fig. 2 shows the measured viscosities of the dispersions of homogeneous nanocubes as a function of ϕ compared with the predicted data obtained using eqn (9) and (10). Even at $\phi = 0.028$ we can observe an overestimation of the simulation data compared with the data predicted by eqn (9). It is also clear that the difference increases with an increase ϕ. The reason for this discrepancy between our simulations and the predicted data is that the interactions between the suspended cubes were ignored in the derivation of eqn (9). The particle interactions become more important with increasing ϕ, such that nonlinear effects need to be considered. In this regard, our simulation results are in good agreement with eqn (10) within the error bars. Based on this plot, we conclude that our method, including the discrete nanocube model, is suitable for studying flow behaviors.

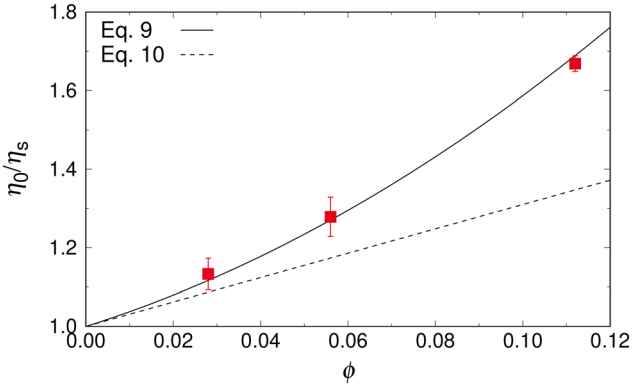

Fig. 2 Normalized zero-shear viscosity, η_0/η_s, of homogeneous cubic dispersions as a function of cube volume fraction, ϕ. Symbols show our simulation data. Solid and dashed lines correspond to regression equation of η_0/η_s–ϕ curve estimated by eqn (9) from ref. 73 and eqn (10) from ref. 41, respectively.

3.2 Patchy nanocubes in suspensions

3.2.1 Pure suspension (one-patch nanocubes). The bonded one-patch cubes have no exposed solvophobic surfaces; thus, only small dimers can be realized in the system. Therefore, we first studied a pure suspension of one-patch cubes that is, $f = 1.0$ to determine the effect of their small dimers on the flow behavior before studying the binary mixtures of one- and two-patch nanocubes. After the system reached equilibrium, the shear was applied. To characterize the strength of the applied shear, we introduce the Péclet number,

$$Pe = \dot{\gamma} d^2/D_0, \tag{11}$$

where D_0 is the translational self-diffusion coefficient of the homogeneous nanocubes obtained by measuring the mean square displacement of the nanocube centers of mass $\Delta R^2(t) = \langle [\mathbf{R}_i(t_0 + t) - \mathbf{R}_i(t_0)]^2 \rangle$ as a function of time, in combination with the relationship $\Delta R^2(t) = 6Dt$. The applied shear rates, $\dot{\gamma}$, ranged from $5.2 \times 10^{-5}\tau^{-1}$ to $1.4 \times 10^{-2}\tau^{-1}$ thus, Pe ranged from 2 to 680.

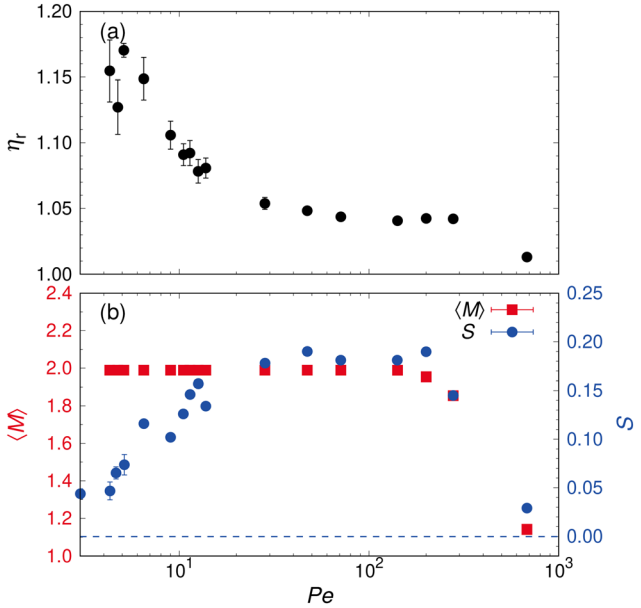

Fig. 3 (a) Relative viscosity, η_r, (b) mean aggregation number, $\langle M \rangle$, and second Legendre polynomial, S, of the dispersion of one-patch nanocubes as a function of Péclet number, Pe, at ϕ = 0.112. The dashed line in panel (b) indicates S at equilibrium.

Fig. 3(a) shows the relative shear viscosity η_r as a function of Pe at ϕ = 0.112. Here, η_r is defined as the ratio of the viscosity of the suspensions of patchy nanocubes to the zero-shear viscosity η_0 of dispersions of homogeneous nanocubes at the same volume fraction ϕ. By introducing η_r, we can extract only the effect of self-assembly on the viscosity changes while excluding the viscosity increase due to the increase in ϕ (see Fig. 2). At low shear rates, $Pe \lesssim 5$, the suspensions exhibited a Newtonian shear response with $\eta_r(\dot{\gamma} \to 0) = 1.15 \pm 0.24$ but then showed distinct shear thinning for $5 \lesssim Pe \lesssim 50$. When Pe was further increased ($50 \lesssim Pe \lesssim 300$), η_r remained approximately constant, followed by shear thinning again with $\eta_r \to 1$ at high shear ($Pe \gtrsim 300$).

In an attempt to more clearly understand the shear-induced viscosity changes in a pure suspension of one-patch cubes, we computed the mean aggregation number $\langle M \rangle = \sum_i^N MP(M)$, where $P(M)$ is the probability of finding a nanocube in an aggregate of M cubes. The cluster size distribution $P(M)$ was quantified by performing a cluster analysis using the density-based spatial clustering algorithm (DBSCAN).[74] Based on previous studies,[49,50] nanocubes were assigned to the same cluster if the distance between the centers-of-mass of their solvophobic patches was less than $1.5a_v$. We also computed the second Legendre polynomial S to investigate the effect of the alignment of the anisotropic clusters caused by the applied shear on the shear viscosity of the suspensions:

$$S = \langle P_2(\cos\theta_i) \rangle = \frac{1}{N}\sum_{i=1}^{N} P_2(\cos\theta_i), \quad (12)$$

where $P_2(\cos\theta_i)$ is the second Legendre polynomial, given by

$$P_2(\cos\theta) = \frac{3}{2}\left\{(n\cdot\Omega_i)^2 - \frac{1}{3}\right\}. \quad (13)$$

In this study, $\mathbf{n}$ is a unit basis in the x direction and $\mathbf{\Omega}$ is an orientation vector from a solvophobic patch to the opposite patch. The order parameter S has an upper bound of 1, corresponding to complete alignment along the x-axis, and a lower bound of −0.5, representing configurations in the plane perpendicular to the x-axis. A value of S = 0 indicates that the clusters have no preferred orientation with respect to flow direction. Fig. 3(b) shows $\langle M \rangle$ and S of the one-patch nanocubes as a function of Pe at ϕ = 0.112. For a wide range of flow regimes ($Pe \lesssim 200$), the dimers (M = 2) remained approximately constant, followed by a distinct breakup of their clusters at high shear. Our previous simulations[61] of Janus sphere dispersions reported that shear-thinning was accompanied by a gradual breakup of the clusters; however, the pure suspension of one-patch cubes showed a decrease in η_r even under weak shear. This shear-thinning behavior for low Pe values originates from the alignment of the dimer clusters along the flow direction. The order parameter gradually increases from S = 0.0 to ≈0.2 as Pe increases to $Pe \approx 40$. Similar shear-thinning behavior induced by the alignment of rod-like colloids has also been observed in previous studies;[75,76] thus, dimer clusters consisting of one-patch nanocubes behave essentially as rod-like colloids until they break up into free particles. For $40 \lesssim Pe \lesssim 200$, the alignment appeared to saturate and remained approximately constant at $S \approx 0.2$, and the suspensions exhibited Newtonian-like behavior with $\eta_r \approx$ constant. When sufficiently strong shear was applied ($Pe \gtrsim 200$), the order parameter gradually decreased to $S \approx 0$, indicating a random orientation of the nanocubes, as the anisotropic shape characteristics were lost by breaking into free particles (M = 1) (see Fig. 3(b)). In this flow regime, clusters eventually broke up, and both $\langle M \rangle$ and η_r approached unity. These results indicate that the shear viscosity of the dispersion is strongly correlated with the mean aggregation number of the clusters, $\langle M \rangle$, after the alignment of the dimer clusters is saturated.

3.2.2 Binary mixtures. Next, we studied the binary mixtures of one- and two-patch nanocubes at f = 0.5. In our recent study,[49] the equilibrium self-assembly of mixtures of one- and two-patch nanocubes was studied in detail. Interestingly, $\langle M \rangle$ and $P(M)$ do not depend on the specific spatial arrangement of the solvophobic faces on the two patch cubes, whereas the patch arrangement mainly affects cluster shape. In Fig. 4(a), we plot the cluster size distributions $P(M)$ in equilibrium. The distributions for the different two-patch cube types seem to be essentially identical within our measurement error, as reflected by the similar values of $\langle M \rangle = 6.0 \pm 0.1$ for type I and $\langle M \rangle = 5.7 \pm 0.4$ for type II at ϕ = 0.112. We also found that a distinct peak at M = 2 appeared for all the investigated ϕ values (the case of ϕ = 0.028 is not shown in Fig. 4(a)). With increasing ϕ, larger

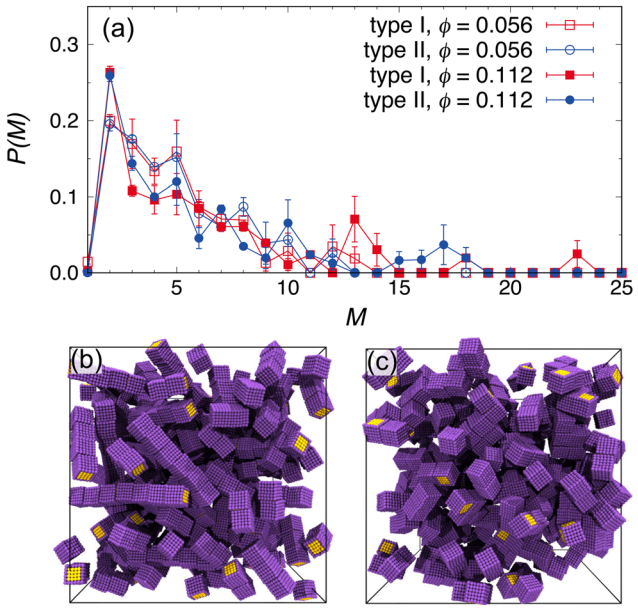

Fig. 4 (a) Cluster size distributions, $P(M)$, in mixtures of one- and two-patch cubes for f = 0.5 at (a) equilibrium state (Pe = 0). (b and c) Equilibrium snapshots of binary mixtures for (b) type I and (c) type II at ϕ = 0.112. Solvent particles are eliminated for clarity.

clusters were observed, *e.g.*, the peak at $M > 15$, which corresponded to a system-spanning cluster appearing at ϕ = 0.112 (Fig. 4(b and c)).

The steady-state morphologies and viscosity behavior under shear are then discussed. Fig. 5(a and b) shows the relative shear viscosity, η_r, and mean aggregation number, $\langle M \rangle$ of mixtures of one- and two-patch cubes (type I) at f = 0.5 as a function of the Péclet number, Pe. At low particle concentrations, ϕ = 0.028 and η_r remained approximately constant for $Pe \lesssim 300$ and weak shear-thinning appeared for $Pe \gtrsim 300$. Interestingly, although the suspension behaved as a Newtonian fluid for the entire range of Pe, the mean aggregation number decreased from $\langle M \rangle \approx 4$ to $\langle M \rangle \approx 2$, indicating that the decomposition of the cluster into dimers from small rod-shaped clusters ($\langle M \rangle \approx 4$) had no significant effect on η_r. At higher particle concentrations (ϕ = 0.056), the suspensions exhibit Newtonian-like behavior for $Pe \lesssim 10$. We observed the first shear-thinning regime at $10 \lesssim Pe \lesssim 60$ with a slight decrease in $\langle M \rangle$. For $60 \lesssim Pe \lesssim 300$, the suspension behaved as a Newtonian fluid, as shown at ϕ = 0.028. For stronger shear, $Pe \gtrsim 300$, a second regime of shear-thinning appeared with a decreasing cluster size from $\langle M \rangle \approx 2$ (small dimers) to $\langle M \rangle \approx 1$ (free cubes). Although the mean aggregation number increased slightly from $\langle M \rangle \approx 4.5$ at ϕ = 0.056 to $\langle M \rangle \approx 6.6$ at ϕ = 0.112, the dense system with ϕ = 0.112 exhibited different behavior, particularly for a small $Pe \lesssim 10$. We can see an obvious increase in $\eta_r \approx 1.35$ compared with the more dilute systems, as shown in Fig. 5(a). To investigate in detail why a ϕ-dependent increase in η_r occurred, we plotted $P(M)$ at ϕ = 0.112 for various Pe values in Fig. 6. Even under weak shear ($Pe \lesssim 10$), the peak of $P(M)$ in

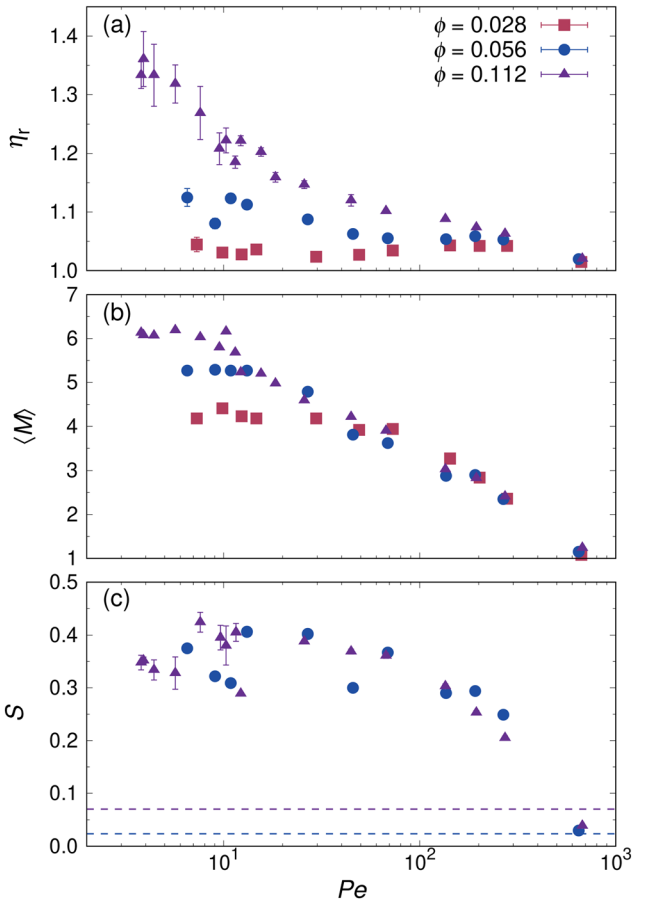

Fig. 5 (a) Relative viscosity, η_r, (b) mean aggregation number, $\langle M \rangle$, and (c) second Legendre polynomial, S, of mixtures of one- and two-patch cubes (type I) at f = 0.5 as a function of the Péclet number, Pe for various volume fractions ϕ, as indicated. The two dashed lines in panel (c) indicate S in equilibrium.

the relatively large rod-shaped clusters ($M \gtrsim 10$) remained [*cf.* Fig. 4(a) and (b)]. The shape anisotropy of these large clusters potentially leads to stronger shear resistance at low Pe.[75,76] Interestingly, although the size and shape of the clusters

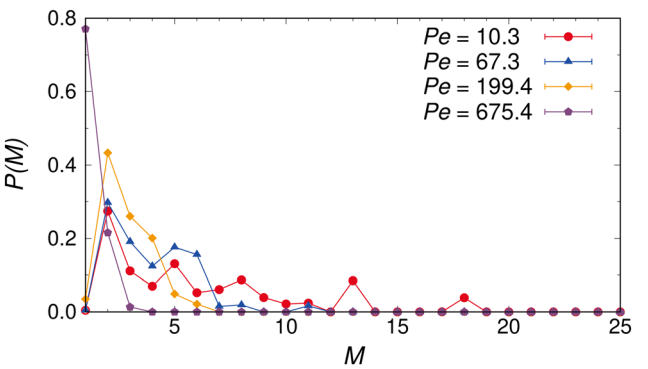

Fig. 6 Cluster size distributions, $P(M)$, in sheared mixtures of one- and two-patch cubes (type I) at ϕ = 0.112 for various Péclet numbers, Pe, as indicated.

remain unchanged when $Pe \lesssim 10$, the relative viscosity gradually decreases to $\eta_r \approx 1.2$. To understand the first shear-thinning regime, we plotted it in Fig. 5(c), the second Legendre polynomial S as a function of Pe. Here, $\boldsymbol{\Omega}$ is defined as the unit vector connecting two different patches of a nanocube in a type I patch arrangement. As the shear increased to $Pe \approx 10$, the clusters gradually became oriented parallel to the flow direction from a random orientation (purple dashed line in Fig. 5(c)). The values of saturated S in the binary mixtures were also found to be larger than those for the pure suspension of one-patch cubes (*cf.* Fig. 3(b) and 5(c), respectively). This indicates that the longer rod-like clusters attain a more aligned configuration until cluster break-up, which is largely the same behavior as previous observations.[61] We also observed shear-induced alignment of clusters in a more dilute suspension ($\phi = 0.056$), but shear-thinning did not appear. We surmise that the effect of the alignment on η_r was not observed for $\phi \lesssim 0.056$ because of the lack of formation of large rod-like clusters ($M > 15$). For $10 \lesssim Pe \lesssim 70$, we observe a gradual breakup of the clusters accompanied by shear-thinning. In this flow regime, the peak of $P(M)$ shifts to lower M values as Pe increases, as shown in Fig. 6. A distinct peak exists at $M = 2$ until it breaks up into single cubes, indicating the high stability of the dimer clusters against shear. When Pe was further increased, the suspensions showed essentially the same behavior as the dilute suspensions, that is, a nearly Newtonian response for $70 \lesssim Pe \lesssim 300$ and shear-thinning with breakage into single cubes for $Pe \gtrsim 300$.

We continue our discussion using a mixture of one- and two-patch cubes (type II). Fig. 7(a) and (b) show η_r and $\langle M \rangle$ as functions of Pe, respectively. For $\phi \leq 0.056$, the suspensions exhibited Newtonian-like behavior for the entire range of Pe numbers and shear-thinning behavior for $Pe \gtrsim 300$, similar to the previously discussed type I patch arrangement.

For higher particle concentrations ($\phi = 0.112$), the increase was ≈35% in η_r, which was almost the same as that for the type I patch arrangement. These results indicate that the increase in η_r appears to be largely independent of the shape of the clusters for all investigated ϕ. A comparison of Fig. 5(b) and 7(b), informs us that M of the mixture with type II cubes remains constant for a wider range of Pe. To obtain a detailed understanding of the differences in cluster stability, we performed additional simulations of isolated clusters consisting of M amphiphilic nanocubes of both types (50 independent runs per M). Fig. 8 shows the bonding energy per nanocubes E_{LJ}/M for aggregates composed of M nanocubes. For both types, E_{LJ}/M decreases with increasing M, and then does not decrease significantly for larger clusters $M > 10$. We also found that E_{LJ}/M of type II cubes is consistently higher than that of type I cubes, indicating that clusters composed of type II cubes are more resistant to shear. The suspensions at $\phi = 0.112$ exhibited shear-thinning for $Pe \lesssim 7$ and then a Newtonian-like response for $7 \lesssim Pe \lesssim 20$, although $\langle M \rangle$ remained unchanged. Similar to type I, the possibility exists that the shear-induced alignment of clusters

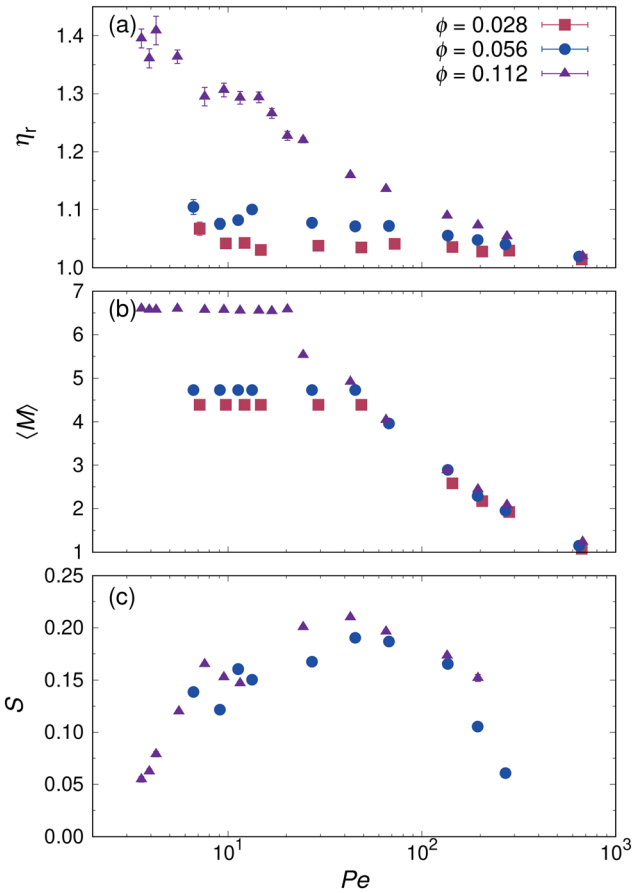

Fig. 7 Same as Fig. 5 but for mixtures of one- and two-patch cubes (type II).

along the flow direction leads to shear-thinning. We also observed that dimer clusters, which can lead to weak shear thinning (see Fig. 3) are the most abundant in the system, as shown in Fig. 9. In Fig. 7(c), we plotted S of clusters, where the orientation of the clusters is defined as the eigenvector with the largest eigenvalue of the gyration tensor. The values of saturated S in binary mixtures with type II cubes were also

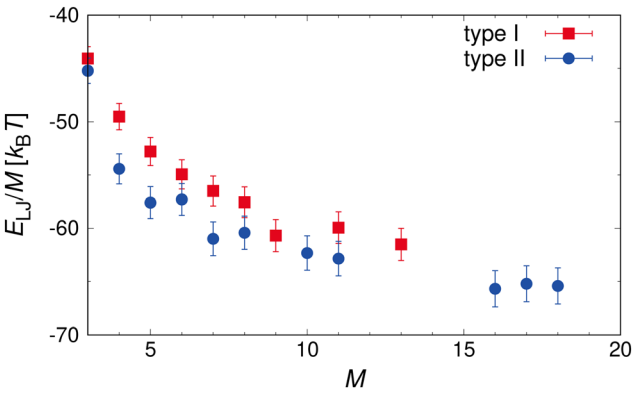

Fig. 8 Bonding energy per particle in equilibrium for clusters consisting of M cubes.

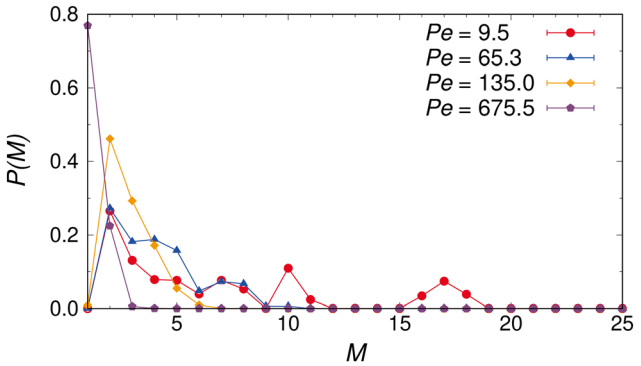

Fig. 9 Cluster size distributions, $P(M)$, in sheared mixtures of one- and two-patch cubes (type II) at ϕ = 0.112 for various Péclet numbers, Pe, as indicated.

found to be lower than those in mixtures with type I cubes, which was attributed to the low shape anisotropy of clusters composed of type II cubes compared to complete rod assemblies composed of type I cubes. From these results, we conclude that the first regime of shear-thinning at $Pe \lesssim 7$ is primarily due to shear-induced alignment of the clusters. However, the alignment effect is weaker than that of the longer rods, as seen in the type I case, thus the decrease in η_r is limited to 10%, followed by Newtonian-like behavior for $7 \lesssim Pe \lesssim 20$. For $Pe \gtrsim 20$, we again observed shear-thinning accompanied by a gradual breakup of clusters. This observation is consistent with the previous findings for mixtures with type I cubes.

4 Conclusions

We employed hybrid molecular dynamics (MD) simulations combined with multiparticle collision dynamics (MPCD) to investigate the structure formation and rheological properties of amphiphilic patchy nanocubes at equilibrium and under shear. We studied a pure suspension of one-patch nanocubes and two binary mixtures of one- and two-patch nanocubes with different patch arrangements at three volume fractions (ϕ = 0.028, 0.056, and 0.112) in the liquid regime of the phase diagram.

For a pure suspension of one-patch cubes, we found three different regimes of shear-induced structure formation, associated with the mean aggregation number, $\langle M \rangle$, and the order parameter. First, at a low shear rate, the dimers composed of one-patch cubes maintain their shape and size ($\langle M \rangle$ = 2), and tend to align along the flow direction as the shear is increased. The resulting shear-thinning behavior was mainly due to the shear-induced alignment of the dimers. The alignment then became saturated, resulting in Newtonian-like behavior. Finally, the dimers break up into free particles when strong shear is applied, and the anisotropic shape characteristics are lost. In this regime, the shear viscosity of the dispersion correlates strongly with $\langle M \rangle$; thus, shear-thinning occurs again.

For binary mixtures of one- and two-patch nanocubes, the resulting cluster shapes, including elongated rods and fractal objects, could be controlled by patch arrangements on the two-patch cubes. In the sheared mixtures, the rod-shaped clusters were more aligned with the flow direction than the fractal-shaped clusters, resulting in distinct shear-thinning for weak shear. Fractal-shaped clusters were also found to be more resistant to shear than rod-shaped clusters. Interestingly, despite the differences in the shape and resistance of the clusters, both suspensions exhibited a similar increase in shear viscosity (≈35%) compared with the homoparticle dispersions. We also found that the binary mixtures exhibited rheological behavior essentially similar to that of a pure suspension of one-patch cubes; therefore, the relationship between structure formation and viscosity obtained in a pure suspension of one-patch cubes is also applicable to binary mixtures of one- and two-patch cubes. This indicates that the design of the patch arrangements on the two-patch cubes primarily affects the flow behavior at low shear rates.

Overall, this study demonstrated the correlation between the rheological properties of suspensions and the design of patchy nanocubes and their self-assembled structures, including shear-induced structural changes. In contrast to systems consisting of patchy spheres or nanorods, the rheological properties of patchy nanocubes are of particular interest because of their significant correlation not only with the cluster size but also with the orientational ordering of clusters. The unique aggregation morphologies and rheological behaviors of such patchy nanocubes cannot be achieved using purely repulsive or attractive nanocubes. The information presented in this paper is also valuable for identifying the synthesis conditions required to obtain novel materials with desired properties and functionalities. In future studies, we aim to extend this approach to and test it on anisotropic particles with other shapes, as other faceted nanoparticles such as tetrahedrons or icosahedrons may also exhibit undiscovered aggregation morphologies and peculiar transport properties through the introduction of patches.

Author contributions

Takahiro Ikeda: investigation, formal analysis, visualization, writing – original draft. Yusei Kobayashi: investigation, methodology, conceptualization, project administration, visualization, writing – original draft, writing – review & editing. Masashi Yamakawa: writing – review & editing, supervision.

Conflicts of interest

The authors declare no conflict of interest.

Acknowledgements

This study was supported by a grant from Japan Science and Technology Agency (JST), Support for Pioneering Research Initiated by the Next Generation (SPRING) Grant Number

JPMJSP2107. Y. K. acknowledges the support of KIT Grants-in-Aid for Early-Career Scientists.

References

1 C. Dai, Y. Huang, X. Lyu, L. Li, Y. Sun, M. Zhao, G. Zhao and Y. Wu, *Chem. Eng. Sci.*, 2019, **195**, 51–61.
2 F. Shi, J. Wu and B. Zhao, *Materials*, 2019, **12**, 1093.
3 Z. Hu, L. Al-Ameri, J. Gardy, M. Alhreez and D. Wen, *Energy Fuels*, 2022, **36**, 12986–12996.
4 Z. Shen, D. T. Loe, J. K. Awino, M. Kröger, J. L. Rouge and Y. Li, *Nanoscale*, 2016, **8**, 14821–14835.
5 J. Xie, Q. Shen, K. Huang, T. Zheng, L. Cheng, Z. Zhang, Y. Yu, G. Liao, X. Wang and C. Li, *ACS Nano*, 2019, **13**, 5268–5277.
6 S. Sivagnanam, K. Das, M. Basak, T. Mahata, A. Stewart, B. Maity and P. Das, *Nanoscale Adv.*, 2022, **4**, 1694–1706.
7 E. Ortel, S. Sokolov, C. Zielke, I. Lauermann, S. Selve, K. Weh, B. Paul, J. Polte and R. Kraehnert, *Chem. Mater.*, 2012, **24**, 3828–3838.
8 B. Yang, L. Leclercq, V. Schmitt, M. Pera-Titus and V. Nardello-Rataj, *Chem. Sci.*, 2019, **10**, 501–507.
9 K. Xiao, J. Cheng, X. Xie, M. Wang, S. Xing, Y. Liu, T. Hartman, D. Fu, K. Bossers, M. A. van Huis, A. van Blaaderen, Y. Wang and B. M. Weckhuysen, *Nat. Mater.*, 2022, **21**, 572–579.
10 R. Lanfranco, P. K. Jana, G. Bruylants, P. Cicuta, B. M. Mognetti and L. D. Michele, *Nanoscale*, 2020, **12**, 18616–18620.
11 W. G. Kim, J. M. Lee, Y. Yang, H. Kim, V. Devaraj, M. Kim, H. Jeong, E. J. Choi, J. Yang, Y. Jang, T. Badloe, D. Lee, J. Rho, J. T. Kim and J. W. Oh, *Nano Lett.*, 2022, **22**, 4702–4711.
12 T. Sato, K. Esashika, E. Yamamoto, T. Saiki and N. Arai, *Int. J. Mol. Sci.*, 2022, **23**, 8807.
13 Y. Wang, Y. Wang, D. R. Breed, V. N. Manoharan, L. Feng, A. D. Hollingsworth, M. Weck and D. J. Pine, *Nature*, 2012, **491**, 51–55.
14 L. Feng, R. Dreyfus, R. Sha, N. C. Seeman and P. M. Chaikin, *Adv. Mater.*, 2013, **25**, 2779–2783.
15 A. J. A. Diaz, J. S. Oh, G. R. Yi and D. J. Pine, *Proc. Natl. Acad. Sci. U. S. A.*, 2020, **117**, 10645–10653.
16 G. Yao, J. Li, Q. Li, X. Chen, X. Liu, F. Wang, Z. Qu, Z. Ge, R. P. Narayanan, D. Williams, H. Pei, X. Zuo, L. Wang, H. Yan, B. L. Feringa and C. Fan, *Nat. Mater.*, 2020, **19**, 781–788.
17 R. Khalaf, A. Viamonte, E. Ducrot, R. Mérindol and S. Ravaine, *Nanoscale*, 2023, **15**, 573–577.
18 Q. Chen, S. Bae and S. Granick, *Nature*, 2011, **469**, 381–384.
19 Y. Taniguchi, M. A. B. Sazali, Y. Kobayashi, N. Arai, T. Kawai and T. Nakashima, *ACS Nano*, 2017, **11**, 9312–9320.
20 Y. Taniguchi, T. Takishita, Y. Kobayashi, N. Arai, T. Kawai and T. Nakashima, *Europhys. Lett.*, 2017, **118**, 68001.
21 D. Zámbó, D. Kovács, G. Södi and A. Deák, *Part. Part. Syst. Charact.*, 2023, **40**, 2200197.
22 L. Cademartiri and K. Bishop, *Nat. Mater.*, 2015, **14**, 2–9.
23 H. Tanaka, T. Dotera and S. T. Hyde, *ACS Nano*, 2023, **17**, 15371–15378.
24 L. Liang, L. Wu, P. Zheng, T. Ding, K. Ray and I. Barman, *JACS Au*, 2023, **3**, 1176–1184.
25 A. Neophytou, D. Chakrabarti and F. Sciortino, *Proc. Natl. Acad. Sci. U. S. A.*, 2021, **118**, e2109776118.
26 S. C. Glotzer and M. J. Solomon, *Nat. Mater.*, 2007, **6**, 557.
27 M. Jones, R. Macfarlane, B. Lee, J. Zhang, K. L. Young, A. J. Senesi and C. A. Mirkin, *Nat. Mater.*, 2010, **9**, 913–917.
28 T. Wang, J. Zhuang, J. Lynch, O. Chen, Z. Wang, X. Wang, D. Lamontagne, H. Wu, Z. Wang and Y. C. Cao, *Science*, 2012, **338**, 358–363.
29 G. Lagaly and S. Ziesmer, *Adv. Colloid Interface Sci.*, 2003, **100–102**, 105–128.
30 L. J. Michot, I. Bihannic, K. Porsch, S. Maddi, C. Baravian, J. Mougel and P. Levitz, *Langmuir*, 2004, **20**, 10829–10837.
31 M. W. Beijerinck, *Verhandelingen der Koninklijke Nederlandsche Akademie van Wetenschappen. Afdeeling Natuurkunde, Sectie 2. Amsterdam*, 1898, **5**, 3–21.
32 F. C. Bawden, N. W. Pirie, J. D. Bernal and I. Fankuchen, *Nature*, 1936, **138**, 1051.
33 J. W. Kim, R. J. Larsen and D. A. Weitz, *J. Am. Chem. Soc.*, 2006, **128**, 14374–14377.
34 K. Bian, H. Schunk, D. Ye, A. Hwang, T. S. Luk, R. Li, Z. Wang and H. Fan, *Nat. Commun.*, 2018, **9**, 2365.
35 Y. H. Lee, C. L. Lay, W. Shi, Y. Lee, H. K. Yang, S. Li and X. Y. Ling, *Nat. Commun.*, 2018, **9**, 2769.
36 A. Bo, Y. Liu, B. Kuttich, T. Kraus, A. Widmer-Cooper and N. de Jonge, *Adv. Mater.*, 2022, **34**, 2109093.
37 D. Gandia, L. Gandarias, L. Marcano, I. Orue, D. Gil-Cartón, J. Alonso, A. García-Arribas, A. Muela and M. L. Fdez-Gubieda, *ACS Nano*, 2022, **16**, 7398–7408.
38 B. S. John, A. Stroock and F. A. Escobedo, *J. Chem. Phys.*, 2004, **120**, 9383.
39 R. Ni, A. P. Gantapara, J. de Graaf, R. van Roij and M. Dijkstra, *Soft Matter*, 2012, **8**, 8826–8834.
40 F. Smallenburg, L. Filion, M. Marechal and M. Dijkstra, *Proc. Natl. Acad. Sci. U. S. A.*, 2012, **109**, 17886–17890.
41 C. D. Cwalina, K. J. Harrison and N. J. Wagner, *Soft Matter*, 2016, **12**, 4654–4665.
42 J. Chen and N. Seeman, *Nature*, 1991, **350**, 631–633.
43 Y. Zhang, F. Lu, K. G. Yager, D. van der Lelie and O. Gang, *Nat. Nanotechnol.*, 2013, **8**, 865–872.
44 K. J. Si, D. Sikdar, Y. Chen, F. Eftekhari, Z. Xu, Y. Tang, W. Xiong, P. Guo, S. Zhang, Y. Lu, Q. Bao, W. Zhu, M. Premaratne and W. Cheng, *ACS Nano*, 2014, **8**, 11086–11093.
45 F. Lu, T. Vo, Y. Zhang, A. Frenkel, K. G. Yager, S. Kumar and O. Gang, *Sci. Adv.*, 2019, **5**, eaaw2399.
46 G. Chen, K. J. Gibson, D. Liu, H. C. Rees, J. H. Lee, W. Xia, R. Lin, H. L. Xin, O. Gang and Y. Weizmann, *Nat. Mater.*, 2019, **18**, 169–174.
47 B. H. Lee and G. Arya, *Nanoscale*, 2019, **11**, 15939–15957.
48 B. H. Lee and G. Arya, *Nanoscale*, 2022, **14**, 3917–3928.
49 Y. Kobayashi and A. Nikoubashman, *Langmuir*, 2022, **38**, 10642–10648.
50 T. Yokoyama, Y. Kobayashi, N. Arai and A. Nikoubashman, *Soft Matter*, 2023, **19**, 6480–6489.

51 A. Malevanets and R. Kapral, *J. Chem. Phys.*, 1999, **110**, 8605–8613.
52 G. Gompper, T. Ihle, D. Kroll and R. G. Winkler, *Adv. Polym. Sci.*, 2009, **221**, 1–87.
53 M. P. Howard, A. Nikoubashman and J. C. Palmer, *Curr. Opin. Chem. Eng.*, 2019, **23**, 34–43.
54 W.-B. Zhang, X.-L. Wu, G.-Z. Yin, Y. Shao and S. Z. D. Cheng, *Mater. Horiz.*, 2017, **4**, 117–132.
55 Y. M. Wani, P. G. Kovakas, A. Nikoubashman and M. P. Howard, *J. Chem. Phys.*, 2022, **156**, 024901.
56 W. Humphrey, A. Dalke and K. Schulten, *J. Mol. Graphics*, 1996, **14**, 33–38.
57 H. C. Andersen, D. Chandler and J. D. Weeks, *J. Chem. Phys.*, 1972, **56**, 3812–3823.
58 C.-C. Huang, A. Chatterji, G. Sutmann, G. Gompper and R. G. Winkler, *J. Comput. Phys.*, 2010, **229**, 168.
59 V. Dahirel, X. Zhao, B. Couet, G. Batôt and M. Jardat, *Phys. Rev. E*, 2018, **98**, 053301.
60 T. Ihle and D. M. Kroll, *Phys. Rev. E: Stat., Nonlinear, Soft Matter Phys.*, 2001, **63**, 020201.
61 Y. Kobayashi, N. Arai and A. Nikoubashman, *Soft Matter*, 2020, **16**, 476–486.
62 Y. Kobayashi, N. Arai and A. Nikoubashman, *Langmuir*, 2020, **36**, 14214–14223.
63 M. P. Allen and D. J. Tildesley, *Computer Simulation of Liquids*, Oxford University Press, USA, 1989.
64 J. A. Anderson, C. D. Lorenz and A. Travesset, *J. Comput. Phys.*, 2008, **227**, 5342–5359.
65 J. Glaser, T. D. Nguyen, J. A. Anderson, P. Liu, F. Spiga, J. A. Millan, D. C. Morse and S. C. Glotzer, *Comput. Phys. Commun.*, 2015, **192**, 97–107.
66 M. P. Howard, A. Z. Panagiotopoulos and A. Nikoubashman, *Comput. Phys. Commun.*, 2018, **230**, 10–20.
67 J. A. Anderson, J. Glaser and S. C. Glotzer, *Comput. Mater. Sci.*, 2020, **173**, 109363.
68 **https://github.com/mphoward/azplugins**.
69 F. Müller-Plathe, *Phys. Rev. E: Stat. Phys., Plasmas, Fluids, Relat. Interdiscip. Top.*, 1999, **59**, 4894–4898.
70 V. Doyeux, S. Priem, L. Jibuti, A. Farutin, M. Ismail and P. Peyla, *Phys. Rev. Fluids*, 2016, **1**, 043301.
71 A. Einstein, *Ann. Phys.*, 1906, **324**, 289.
72 A. Einstein, *Ann. Phys.*, 1911, **339**, 591.
73 R. K. Mallavajula, D. L. Koch and L. A. Archer, *Phys. Rev. E: Stat., Nonlinear, Soft Matter Phys.*, 2013, **88**, 052302.
74 M. Ester, H.-P. Kriegel, J. Sander and X. Xu, *Proc. Second Int. Conf. Knowl. Discov. Data Min.*, 1996, vol. 96, p. 226.
75 C. Lang, J. Kohlbrecher, L. Porcar, A. Radulescu, K. Sellinghoff, J. K. G. Dhont and M. P. Lettinga, *Macromolecules*, 2019, **52**, 9604–9612.
76 C. Lang and M. P. Lettinga, *Macromolecules*, 2020, **53**, 2662–2668.